

Unified Timing Analysis for Closed-Loop Goal-Oriented Wireless Communication

Lintao Li, Anders E. Kalør, *Member, IEEE*, Petar Popovski, *Fellow, IEEE*, and Wei Chen, *Senior Member, IEEE*

Abstract—Goal-oriented communication has become one of the focal concepts in sixth-generation communication systems owing to its potential to provide intelligent, immersive, and real-time mobile services. The emerging paradigms of goal-oriented communication constitute closed loops integrating communication, computation, and sensing. However, challenges arise for closed-loop timing analysis due to multiple random factors that affect the communication/computation latency, as well as the heterogeneity of feedback mechanisms across multi-modal sensing data. To tackle these problems, we aim to provide a unified timing analysis framework for closed-loop goal-oriented communication (CGC) systems over fading channels. The proposed framework is unified as it considers computation, compression, and communication latency in the loop with different configurations. To capture the heterogeneity across multi-modal feedback, we categorize the sensory data into the periodic-feedback and event-triggered, respectively. We formulate timing constraints based on average and tail performance, covering timeliness, jitter, and reliability of CGC systems. A method based on saddlepoint approximation is proposed to obtain the distribution of closed-loop latency. The results show that the modified saddlepoint approximation is capable of accurately characterizing the latency distribution of the loop with analytically tractable expressions. This sets the basis for low-complexity co-design of communication and computation.

Index Terms—closed-loop timing analysis, multi-modal feedback, immersive communication, saddlepoint approximation.

I. INTRODUCTION

A. Motivation and Contributions

Driven by the rapid development of information technology and the continuous improvement of hardware capability, the sixth-generation (6G) communication systems are envisioned to fuse the physical and digital worlds by providing intelligent, immersive, and real-time services [1]. This is, for instance, reflected in the IMT-2030 draft for the 6G wireless communication technology [2] published by the International Telecommunication Union (ITU), which in addition to hyper reliable and low-latency communication also includes immersive communication as central 6G usage scenarios.

The work of Lintao Li and Wei Chen was supported by the National Natural Science Foundation of China/Research Grants Council Collaborative Research Scheme under Grant No. 62261160390. The work of A. E. Kalør was supported in part by the Independent Research Fund Denmark (IRFD) under Grant 1056-00006B and in part by the Horizon Europe SNS project “6G-GOALS” (grant 101139232). The work of P. Popovski was supported in part by the Villum Investigator Grant “WATER” from the Velux Foundation, Denmark, and in part by the Horizon Europe SNS project “6G-GOALS” (grant 101139232).

Lintao Li and Wei Chen are with the Department of Electronic Engineering, Tsinghua University, Beijing 100084, China, and also with the Beijing National Research Center for Information Science and Technology, Tsinghua University, Beijing 100084, China (email: llt20@mails.tsinghua.edu.cn; wchen@tsinghua.edu.cn).

Anders E. Kalør and Petar Popovski are with the Department of Electronic Systems, Aalborg University, 9220 Aalborg, Denmark (e-mail: aek@es.aau.dk; petarp@es.aau.dk).

Against this background, the goal-oriented communication paradigm gets significant traction in 6G [3]. Supported by artificial intelligence (AI), goal-oriented communication aims to provide intelligent and immersive experiences for users by optimizing the communication for the receiver’s intention and experience, rather than simply providing reliable, content-blind packet delivery [4], [5]. Combined with Metaverse and Digital Twin (DT) technology, this enables 6G to break the spatial constraints to promote the achievement of the flexible interconnection between the physical world and the digital virtual space [6].

Differently from 5G, goal-oriented paradigms require demanding *closed-loop* interactions with strict timing requirements, starting from the commands transmitted by the user and ending with the reception of feedback. The closed-loop interactions are common in several of the typical 6G scenarios considered by the Third Generation Partnership Project (3GPP) [7], including remote control, virtual social, and gaming. However, the closed-loop timing analysis is challenging compared to the point-to-point perspective that has dominated the literature so far, as it needs to consider processing latency of intermediate notes caused by, e.g., compression and computation. Thus, there is a need to develop a unified timing-analysis framework for closed-loop goal-oriented communication (CGC) systems over wireless channels, which can serve as a tool to ensure that users get the desired real-time experience.

To address this problem, we aim to formulate a unified timing-analysis framework and propose a general method to characterize the closed-loop timing performance in CGC systems while taking into account both communication, computation, and compression latencies. Specifically, we consider a general CGC system with a remote-control task comprising a user (UE), a base station (BS), and a remote agent (RA), which are assumed to operate in a closed loop. The system is exemplified as a robotic scenario with a DT at the BS in Fig. 1. We consider both periodic and sporadic traffic. The periodic traffic, referred to as periodic feedback (PF), is transmitted at fixed intervals from the RA to the UE, representing, e.g., sensor data. The sporadic traffic is initiated by control data transmitted from the UE to the RA, which then responds with event-triggered (ET) data. The communication goes through the BS, which is equipped with a mobile-edge-computing (MEC) server to operate computation tasks, such as feature extraction for AI, compression, and decompression. Note that, although the remote agent is illustrated as a robot, it could also act as a cloud server in a gaming scenario, or as another UE for a virtual social scenario. A key novelty of the proposed model is that it enables closed-loop analysis of heterogeneous multi-modal feedback comprising both event-triggered and periodic feedback, as well as stochastic computation and compression

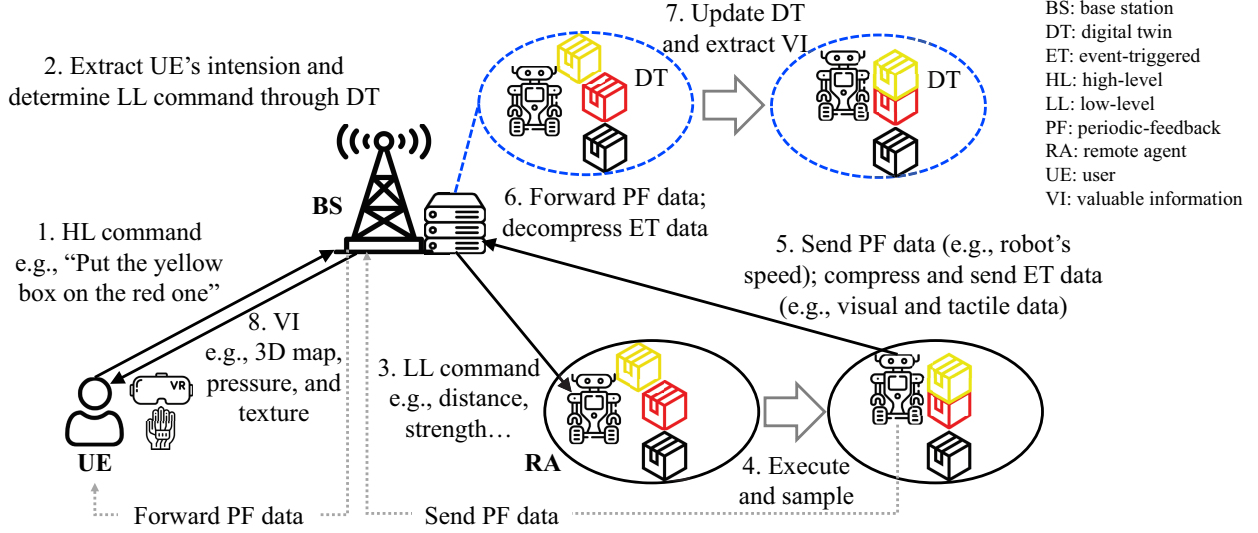


Fig. 1: System model for a general CGC system. This figure shows an example of the remote control with the assistance of MEC, semantic information, and DT. Multiple communication and computation processes are included in this closed loop.

latency. The stochastic nature of the latter has been ignored in most existing work, although these aspects are crucial in end-to-end latency analysis [8]–[10]. Besides, motivated by perceptual requirements of interactive applications [7], [11]–[13], we explicitly model the asynchrony between the transmission latency of PF and ET data, referred to as *jitter*. Further details of the model will be given in Section II.

Note that the model in Fig. 1 is rather general, capable to cover some commonly referred scenarios for CGC systems. For the remote control task shown in Fig. 1, we are interested in the closed-loop latency by accounting for the timeliness of the control data and the jitter of the multi-modal feedback. For the authorization of avatar usage rights, specified by 3GPP in [7], the RA acts as a cloud server. UE sends requests to the cloud server through BS without relying on the computation process at the BS. Once the cloud server receives the requests, it inquires and returns profiles of the avatar to the UE. Meanwhile, authorization information will be sent to UE periodically to authorize the use of the avatar legally. In this scenario, reducing the asynchrony between profile reception and authorization ensures immediate avatar utilization without additional latency. Differently from the remote control, we focus on the closed-loop latency without a specific concern of control link latency.

Using the proposed model, and with consideration of timeliness, jitter, and reliability, we formulate a unified framework of timing analysis for CGC systems, capable of addressing both average- and tail-based timing constraints for CGC systems with different information-processing mechanisms and configurations. To this end, we propose a general saddlepoint-approximation-based method to obtain the analytical expression of the distribution of closed-loop latency with high accuracy. Based on this general method, we also give a corollary for efficiently approximating the conditional expectation in the timing constraints. The proposed methods can be generalized to timing analysis in other closed-loop scenarios.

The main contributions are summarized as follows:

- We formulate a unified timing-analysis framework for

CGC systems with different configurations, which takes the randomness of the computation, compression, and communication latency into account. The formulated framework integrates the timeliness, jitter, and reliability of CGC systems.

- We consider two heterogeneous information flows with both PF and ET data, representing different feedback mechanisms of multi-modal sensing data.
- We propose a general saddlepoint approximation (SPA)-based method for analytically characterizing the timing measures in CGC systems. For specific scenarios, the central limit theorem (CLT) is also introduced to improve the efficiency of the method while ensuring accuracy.
- Based on this method, we derive an efficient approximation for calculating the conditional expectation in timing constraints.

B. Related Work

In [14], a goal-oriented communication and prediction co-design was proposed to improve the reliability of the haptic communication system. The end-to-end communication latency was chosen as the timing metric with a queueing model, while the computation latency is omitted in [14]. Wen *et al.* optimized the discriminant gain to achieve the goal of improving the accuracy of AI inference in an integrated sensing and communication (ISAC) system [15]. Meanwhile, they considered the latency constraint in this system, which focused on the uplink latency comprised of communication, computation, and sensing procedures. The authors of [16] designed resource allocation and computation offloading schemes to minimize the uplink latency of DT-enabled Metaverse. In [15] and [16], the constant computation latency is incorporated into the timing measurements. However, they only considered the one-way latency instead of the closed-loop latency.

Conducting closed-loop timing analysis was proved to be effective for the wireless networked control system (WCNS) in [17] and [18]. Thus, it is important to analyze the timing performance of a goal-oriented communication system from

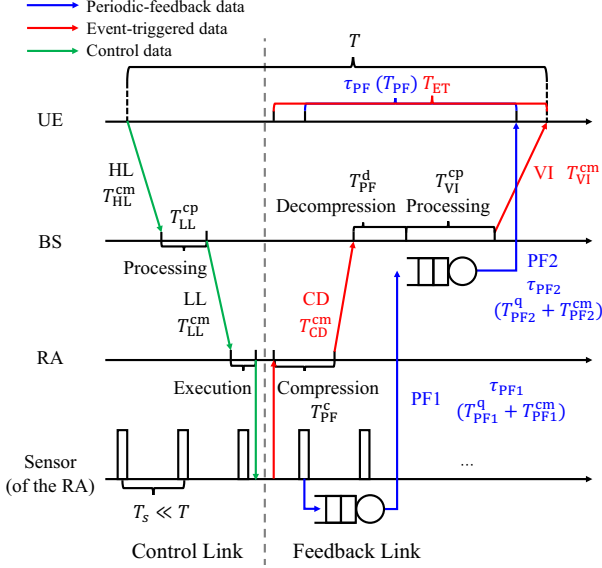


Fig. 2: Diagram of the components of the closed-loop latency. The UE transmits commands to the RA through the control link, and the RA transmits both periodic-feedback and event-triggered sensor data to the UE.

the closed-loop perspective. In [19], the authors carried out the closed-loop timing analysis for wireless federated learning systems by taking both random latency of local information uploading and global model broadcasting into account. However, the computation latency was also assumed as a deterministic term in [19], which ignored its stochastic property [8]–[10]. To address these problems, Suman *et al.* conducted a statistical timing analysis for a closed-loop teleoperation system [8], in which the randomness of computation and compression latency were accounted for. However, the heterogeneity between the multi-modal feedback, which widely exists in various goal-oriented communication, was not considered.

The SPA technique that we apply is a powerful method to approximate complicated distributions with high accuracy guarantees while avoiding intractable computations [20]. SPA has been widely used in communication research. In [19], SPA was used to characterize the distribution of transmission latency in wireless federated learning systems. An efficient SPA-based method for evaluating block error probabilities was proposed in [21], and the power-latency-throughput tradeoff of delay-constrained wireless systems was characterized by SPA in [22].

C. Paper Organization and Notation

The paper is structured as follows. Section II presents the unified timing framework for CGC systems considered in this paper. Section III introduces the latency components and formally defines the overall objective, while Section IV proposes the SPA-based timing analysis for the CGC system. Section V validates the analysis through numerical results, and finally the paper is concluded in Section VI.

Notation: $\mathbb{E}\{x\}$ denotes the expectation of the random variable x , and $\text{Var}\{x\}$ denotes its variance. $f'(x)$ and $f''(x)$ denote the first-order and second-order derivative of $f(x)$, respectively. $\mathcal{N}(0, 1)$ denotes the standard Gaussian distribution with cumulative distribution function (CDF) $\Phi(x) =$

$\frac{1}{\sqrt{2\pi}} \int_{-\infty}^x e^{-\frac{y^2}{2}} dy$ and probability density function (PDF) $\phi(x) = \frac{1}{\sqrt{2\pi}} e^{-\frac{x^2}{2}}$. $\gamma(s, x) = \int_0^x t^{s-1} e^{-t} dt$ is the lower incomplete gamma function, $\{x\}^+ = \max\{x, 0\}$, and $\text{sign}(x)$ denotes the sign of x .

II. A UNIFIED FRAMEWORK FOR TIMING ANALYSIS IN CGC SYSTEMS WITH DIFFERENT CONFIGURATIONS

In this section, we present a unified framework for timing analysis in CGC systems. We first give a system overview, and then introduce the components of latency. The wireless channel model is presented in Section II-C, and Section II-D defines different timing constraints used to formulate the proposed framework with different configurations.

A. System Overview

We study the CGC system depicted in Fig. 1, consisting of a BS, a single UE, and a single RA equipped with a sensor. The UE and the RA communicate over a wireless channel through the BS using dedicated channel resources, and the BS is equipped with an MEC server to perform computation tasks, which include feature extraction and decompression. We will refer to the channel from the UE to the RA as the *control link* (CL), while the link from the RA to the UE is the *feedback link* (FL). The communication flow is detailed in Fig. 2, where we consider three packet types: control data, periodic-feedback (PF) data, and event-triggered (ET) data.

Control data is transmitted sporadically by the UE as high-level (HL) commands, and are assumed to be transmitted at relatively long intervals so that no queuing is needed. For instance, control data could represent the intention of UE to put the yellow box on the red one as shown in Fig. 1. The HL commands are assumed to be much larger than the PF transmissions, and subject to a random processing delay at the BS. Specifically, the UE transmits an HL command to the BS, which then processes the received command to extract the semantic information, e.g., with the help of a large language model [23] and the DT model maintained at the BS. The HL command is assumed to consist of N_{HL} packets of size n_{HL} bits each¹. At the BS, the HL command is turned into detailed control signals, referred to as low-level (LL) commands, which are transmitted from the BS to the RA. The LL commands consist of N_{LL} packets of n_{LL} bits.

PF data usually has a small size, and typically represents numeric values, e.g., the speed of the RA and the temperature of the remote environment [7]. The PF data are collected at fixed, short intervals every T_s seconds, and can be shown on UE's equipment without further processing. However, the data are queued at both the RA and the BS.

Finally, ET data are generated by the RA as a response to an LL command. ET data is usually throughput-intensive and may include multimedia data, e.g., video, tactile details, and audio. Thus, the ET data is first compressed by the RA and then transmitted to the BS. The MEC server at BS decompresses the data, extracts valuable information (VI) from the ET data,

¹There is usually one packet containing the specific command signals. However, the analysis in this paper does not specify the value of the number of packets for both HL and low-level (LL) since the proposed framework and analysis are general.

e.g., the location and texture of the objective, and updates its DT model to prepare for the next loop. After the processing, the valuable information is encoded into N_{VI} packets with equal size n_{VI} bits. Finally, the valuable information will be sent to UE. We denote the total size of the original ET data at the RA as n_{ET} bits. The compressed ET data is transmitted using N_{CD} packets with n_{CD} bits each.

The focus of this paper is on the closed-loop latency, T , of a single transmission round under various constraints on the individual links. Specifically, a single transmission round starts from the transmission of a HL command by the UE and lasts until the UE has received both the corresponding ET data and the PF data generated closest to the time instant at which the LL data is received by the RA. The proposed framework in the following subsections takes the latency requirements for CL and the jitter between two heterogeneous information flows in FL into account. These requirements will affect T by influencing the latency of CL and FL. For the multiple-transmission scenario, more queueing delay is introduced. We leave the analysis of the scenario with multiple transmissions for future work.

B. Latency Components

Based on the previous description and Fig. 2, the transmission latency of the PF data, denoted by T_{PF} , is given by

$$T_{PF} = T_{PF1}^q + T_{PF1}^{cm} + T_{PF2}^q + T_{PF2}^{cm}, \quad (1)$$

where T_{PF1}^q and T_{PF1}^{cm} are the queuing and transmission delays from the RA to the BS, respectively, and T_{PF2}^q and T_{PF2}^{cm} are the queuing and transmission delays from the BS to the UE, respectively. For the control data, the latency from UE to RA can be written

$$T_{CL} = T_{HL}^{cm} + T_{LL}^{cp} + T_{LL}^{cm}, \quad (2)$$

where T_{HL}^{cm} and T_{LL}^{cm} are the transmission delay of the HL command and the LL command, respectively, and T_{LL}^{cp} is the processing delay at the BS. Similarly, the latency of the ET transmission from the RA to the UE is

$$T_{ET} = T_{ET}^c + T_{CD}^{cm} + T_{ET}^d + T_{VI}^{cp} + T_{VI}^{cm}, \quad (3)$$

where T_{ET}^c is the compression delay at the RA, T_{CD}^{cm} and T_{VI}^{cm} are the transmission delay from the RA to the BS and from the BS to the UE, respectively, and T_{ET}^d and T_{VI}^{cp} are the decompression delay and the processing delay at the BS, respectively.

Recall that we are interested in the closed-loop latency from the generation of the HL command until the reception of both the corresponding ET data and the PT data generated closest in time to the generation time of the ET data. Since the interval of the periodic transmission, T_s , is relatively small, its impact is negligible and the latency of the feedback link, denoted as T_{FL} , can thus be approximated by

$$T_{FL} \approx \max \{T_{PF}, T_{ET}\}. \quad (4)$$

Using this, we finally write the closed-loop latency as

$$T = T_{CL} + T_{FL}. \quad (5)$$

Finally, we also define the jitter of the feedback link as the absolute difference between T_{ET} and T_{PF} , i.e., $|T_{ET} - T_{PF}|$.

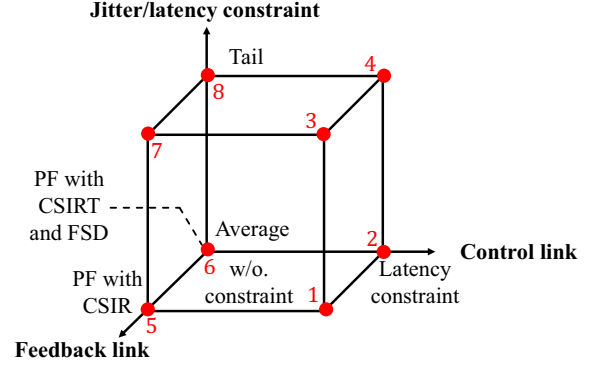


Fig. 3: Configurations considered in the proposed framework.

C. Wireless Channel

We assume independent block fading channels at all links so that the channel gain remains constant over the length of a transmitting packet. Assuming a transmission power of P_i , at link $i \in \{HL, LL, PF1, PF2, CD, VI\}$, the signal-to-noise ratio (SNR) at the receiver is given by

$$SNR_i = \frac{d_i^{-\ell_i} |h_i|^2 P_i}{N_0 B_i}, \quad i \in \{HL, LL, PF1, PF2, CD, VI\}, \quad (6)$$

where $|h_i|^2$ is the small-scale channel power gain, d_i is the distance between the transmitter and the receiver, ℓ_i is the path-loss exponent, N_0 is the spectral density of the noise power, and B_i is the bandwidth. For $i \in \{LL, CD, PF1\}$, d_i refers to the distance between RA and BS, which we denote by d_{RB} . For $i = \{HL, PF2, VI\}$, d_i refers to the distance between BS and UE, which we denote by d_{BU} . Besides, we let ℓ_{BU} denote the path-loss exponent of the link between BS and UE, while ℓ_{RB} denote the path-loss exponent of the link between RA and BS. Moreover, $B_{PF1} = B_{PF2} = B_{PF}$, while $B_{CD} = B_{VI} = B_{ET}$. We are primarily concerned with the case in which channel state information is known only at the receiver side (CSIR), and the transmitter adopts the ϵ_i -outage rate R_i . With $|h_i|^2 \sim \exp(1)$, the relationship between R_i and ϵ_i is given by [24]

$$R_i = B_i \log_2 \left(1 - \frac{d_i^{-\ell_i} P_i}{N_0 B_i} \ln(1 - \epsilon_i) \right). \quad (7)$$

For completeness, we also consider the case where the transmitter also has perfect channel state information for the transmission of PF packets, referred to as CSIRT. In this case, we additionally assume that frequency or spatial diversity (FSD) is available, e.g., through multiple antennas. This is motivated by our previous work [25], [26], which shows that with both CSIRT and FSD, it can be ensured that the delay violation probability is zero with finite average power. In this case, we let τ_{PF} denote the deadline of PF data with CSIRT and FSD, which means the latency of each PF packet cannot be larger than τ_{PF} . Thus, with CSIRT and FSD, we can use τ_{PF} to represent the latency of PF data.² Moreover, we let τ_{PF1} and τ_{PF2} denote the deadline for the PF data transmission

²Though the average power is finite, the required instantaneous power may be large. If there is a maximum power constraint, the delay violation probability of the packet is not zero and can be characterized by large deviation theory [25] and extreme value theory [19]. The analysis of this setting is left for future work.

from RA to BS and BS to UE, respectively, which satisfy $\tau_{PF1} + \tau_{PF2} \leq \tau_{PF}$.

D. A Unified Framework of Timing Constraints for CGC Systems with Different Configurations

In this subsection, we establish a unified timing-analysis framework for CGC systems under different configurations, shown as vertices in Fig. 3. The proposed framework ensures the timeliness performance of CL and the jitter performance of FL to cover general requirements for CGC systems. Meanwhile, these constraints also affect the closed-loop latency T through T_{CL} and T_{FL} to ensure the reliability of CGC systems.

As indicated on the jitter/latency constraint axis, we consider both average and tail-based constraints on jitter and latency. The average-based constraints are related to the expectation of timing measurements, while tail-based constraints here are related to the violation probability of timing measurements. For the control link (CL), which handles the transmission of control data, we consider both with and without a latency constraint representing a timeliness requirement on T_{CL} . Finally, the feedback link (FL) may or may not have CSIRT and FSD for the PF data, as represented by the last axis. When CSIRT and FSD are available, then there is a hard delay constraint for the PF data, τ_{PF} , as mentioned in Section II-C. Therefore, under this condition, we treat the PF transmission latency T_{PF} as deterministic, $T_{PF} = \tau_{PF}$. On the other hand, when only CSIR is available T_{PF} is a random variable.

For the delay jitter, there are two different evaluating methods under different configurations, which correspond to the FL axis in Fig. 3. The first one refers to the case that the transmission of PF data has CSIRT and FSD. In this case, the latency of PF data is characterized by the threshold τ_{PF} . Thus, the jitter is defined as the $|T_{ET} - \tau_{PF}|$.

The second one refers to the case that the transmission of PF data only has CSIR. Thus, the latency of PF data is also stochastic. Then, the jitter is the difference between two random variables, i.e., $|T_{ET} - T_{PF}|$.

Based on these constraints on each axis, we can combine them to form the eight vertices of the cube in Fig. 3.³ Next, we elaborate on each vertex in Fig. 3. Vertices 1-4 refer to interactive systems with control of RA under different configurations as shown in Fig. 1.

- Vertex 1 – average constraints for CL and PF with CSIR:

$$\begin{cases} \mathbb{E}\{T_{CL}\} \leq \varrho_{CL}, \\ \mathbb{E}\{|T_{ET} - T_{PF}|\} \leq \varrho_{FLd}, \end{cases} \quad (8)$$

where ϱ_{CL} is the average latency constraint of CL, and ϱ_{FLd} is the average jitter constraint of FL.

- Vertex 2 – average constraints for CL and PF with CSIRT and FSD:

$$\begin{cases} \mathbb{E}\{T_{CL}\} \leq \varrho_{CL}, \\ \tau_{PF1} + \tau_{PF2} \leq \tau_{PF}, \\ \mathbb{E}\{(T_{ET} - \tau_{PF})^+\} \leq \varrho_{FLs}, \end{cases} \quad (9)$$

³Note that except the constraints on the vertices of the cube, we can also form the constraints such as the combination of tail-based FL constraint and average-based CL constraint. These constraints can be seen as the points between vertices i and $i + 2$, $i \in \{1, 2, 5, 6\}$. Due to the layout limitation, we omit the detailed discussion.

where τ_{PF} and ϱ_{FLs} are average jitter constraints of FL. In this case, we treat the part in which $T_{ET} < \tau_{PF}$ as no jitter. This is because τ_{PF} is deterministic so that both ET and PF feedback can be shown to UE until PF data is received if $T_{ET} < \tau_{PF}$. Note that the third constraint in this case can be rewritten as

$$\mathbb{E}\{T_{ET} - \tau_{PF} | T_{ET} > \tau_{PF}\} \leq \frac{\varrho_{FLs}}{\Pr\{T_{ET} > \tau_{PF}\}}, \quad (10)$$

which can be seen as a condition value-at-risk (CVaR) based constraint [27].

- Vertex 3 – tail constraints for CL and PF with CSIR:

$$\begin{cases} \Pr\{T_{CL} < \tau_{CL}\} \geq \eta_{CL}, \\ \Pr\{|T_{ET} - T_{PF}| < \tau_{td}\} \geq \eta_{td}, \\ \text{Var}\{|T_{ET} - T_{PF}|\} \leq \rho_{td}, \end{cases} \quad (11)$$

where η_{CL} and τ_{CL} are tail latency constraints of CL. τ_{td} , η_{td} , and ρ_{td} are the tail jitter constraint of FL. For the first constraint in Eq. (11), if η_{CL} is given to find the minimum τ_{CL} , τ_{CL} turns into value at risk (VaR) [27], i.e.,

$$\tau_{CL} = \inf_t \{\Pr\{T_{CL} < t\} \geq \eta_{CL}\}. \quad (12)$$

If τ_{CL} is given, solving the maximum value of η_{CL} is equal to minimizing the delay violation probability, i.e.,

$$\eta_{CL} = \inf_p \{\Pr\{T_{CL} \geq \tau_{CL}\} \leq p\}. \quad (13)$$

The second and third constraints in Eq. (11) refer to the tail jitter constraint for FL. Except for the violation probability of $|T_{ET} - T_{PF}|$, the variance of the jitter is also included to cover general cases, which is also an important measurement for tail behavior as shown in [28].

- Vertex 4 – tail constraints for CL and PF with CSIRT and FSD:

$$\begin{cases} \Pr\{T_{CL} < \tau_{CL}\} \geq \eta_{CL}, \\ \tau_{PF1} + \tau_{PF2} \leq \tau_{PF}, \\ \Pr\{T_{ET} < \tau_{PF}\} \geq \eta_{ts}, \\ \text{Var}\{T_{ET} - \tau_{PF}\} \leq \rho_{ts}, \end{cases} \quad (14)$$

where τ_{PF} , η_{ts} and ρ_{ts} are the tail jitter constraints of FL. Since τ_{PF} is a constant, the fourth constraint in this case is equivalent to

$$\text{Var}\{T_{ET}\} \leq \rho_{ts}. \quad (15)$$

- Vertices 5-8 correspond to vertices 1-4 without the first constraint in Eqs. (8), (9), (11), and (14), respectively. In these vertices, there are no specific constraints for the CL. The main focus is on the performance of the closed-loop latency and FL's jitter, which covers the system without the control for RA, e.g., the authorization of avatar usage rights mentioned in Section I-A.

Note that we have to obtain the distributions of T_{PF1}^q and T_{PF2}^q for modeling vertices 1, 3, 5, and 7. However, there is no existing conclusion on the distribution of T_{PF1}^q and T_{PF2}^q to the best of authors' knowledge.⁴ Thus, we mainly focus on the modeling and analysis of vertices 2, 4, 6, and 8 in the following parts, which refer to the case that the transmission of PF data has CSIRT and FSD. Based on the proposed unified framework

⁴Once we have the distribution of T_{PF1}^q and T_{PF2}^q , vertices 1, 3, 5, 7 can be analytically expressed by the proposed method in this paper.

of timing analysis in this paper, more timing metrics can be considered, e.g., age of information and age of loop [17], [18]. Besides, we can also consider the queueing process at the BS and RA sides for ET data with the aid of large deviation theory [29], [30] to denote the asymptotic distribution of queueing latency. We will leave these thoughts in the future work.

III. STOCHASTIC LATENCY COMPONENTS AND A UNIFIED OPTIMIZATION PROBLEM IN CGC SYSTEMS

In this section, we will analyze the distribution of communication, computation, compression, and decompression latency in CGC systems. A unified optimization problem is formulated by combining different kinds of constraints and stochastic latency components.

A. Distributions of Latency Components in CGC Systems

We start with the introduction of the communication latency. The latency of transmitting a packet is denoted by t_i , $i \in \{\text{HL}, \text{LL}, \text{PF1}, \text{PF2}, \text{CD}, \text{VI}\}$, which satisfies $t_i = \frac{n_i}{R_i}$. Thus, the total time for successfully transmitting one packet follows a geometric distribution. As defined in Section II-A, T_i^{cm} denotes the transmission latency of N_i packets. T_i^{cm} follows a negative binomial distribution $\text{NB}(N_i, 1 - \epsilon_i)$. The PDF of T_i^{cm} is given by

$$\Pr\{T_i^{\text{cm}} = (N_i + k)t_i\} = \binom{k + N_i - 1}{N_i - 1} (1 - \epsilon_i)^{N_i} \epsilon_i^k, \quad (16)$$

where $k \in \{0, 1, \dots\}$.

The PF data is collected every T_s seconds. Thus, one packet containing the PF data arrives at the buffer every T_s seconds, which incurs a queueing delay. For vertices 2, 4, 6, and 8, we consider the case that CSIRT and FSD are available for the transmission of PF data. With CSIRT and FSD, the deadline constraint can be met with a finite average power [25]. Specifically, for $j \in \{\text{PF1}, \text{PF2}\}$, the deadline-constrained capacity is approximated by [26], [31]

$$R_j = B_j \log_2 \left(1 + \frac{c_1 d_j^{-\ell_j} P_j}{N_0 B_j (c_2 + (\tau_j)^{-c_3})} \right), \quad (17)$$

where $c_i > 0$, $i \in \{1, 2, 3\}$ are constants. Note that, for the transmission from BS to UE, the arrival of PF data is not periodical. However, we can transform it into periodical arrival by reintegration, i.e., let one packet get into the transmitting buffer even more than one packet arrives in this time slot. Therefore, the conclusion is valid. According to our previous conclusions in [26] and [31], by transmitting the PF data through two antennas with maximum-ratio combining, the closed-form approximation for the deadline-constrained capacity is

$$R_j = B_j \log_2 \left(1 + \frac{2.8771 d_j^{-\ell_j} P_j}{N_0 B_j (1.8771 + (\tau_j)^{-3.411})} \right). \quad (18)$$

By this means, to ensure that all PF data is transmitted within τ_j , the average power P_j can be solved from Eq. (18) by setting $R_j = \frac{n_j}{T_s}$.

Then we introduce the formulation of the computation time. As shown in Fig. 2, there are two feature extraction procedures

in the CGC system, which are calculated at the MEC server. For $l \in \{\text{LL}, \text{VI}\}$, the computation time is given by

$$T_l^{\text{cp}} = \frac{\tilde{n}_l X_l^{\text{cp}}}{\chi_{\text{MEC}}}, \quad (19)$$

where χ_{MEC} is the frequency of the processing unit at the MEC server, and X_l^{cp} is the number of processing-unit cycles required for processing 1-bit data. $\tilde{n}_{\text{LL}} = N_{\text{HL}} n_{\text{HL}}$ and $\tilde{n}_{\text{VI}} = n_{\text{ET}}$. As shown by previous research [8]–[10], the number of cycles allocated to compute 1 bit is stochastic in nature. For the CPU case, X_l^{cp} follows a gamma distribution $\text{Gamma}(\alpha_{\text{MEC}}, \beta_l)$ [8]–[10], where α_{MEC} and β_l are the shape and rate parameters of the gamma distribution, respectively. The shape parameter remains the same for all tasks performed by the same processor, while the scale parameter β_l will be different for different tasks [8]. Thus, the computation time also follows a gamma distribution $\text{Gamma}(\alpha_{\text{MEC}}, \frac{\chi_{\text{MEC}} \beta_l}{\tilde{n}_l})$. The PDF of T_l^{cp} is given by

$$f_l^{\text{cp}}(x) = \frac{(\chi_{\text{MEC}} \beta_l)^{\alpha_{\text{MEC}}}}{\tilde{n}_l^{\alpha_{\text{MEC}}} \Gamma(\alpha_{\text{MEC}})} x^{\alpha_{\text{MEC}}-1} \exp\left(-\frac{\chi_{\text{MEC}} \beta_l}{\tilde{n}_l} x\right), \quad (20)$$

where $x > 0$. The expectation of T_l^{cp} is $\mu_l^{\text{cp}} = \frac{\tilde{n}_l \alpha_{\text{MEC}}}{\chi_{\text{MEC}} \beta_l}$, while its variance is $\xi_l^{\text{cp}} = \frac{\tilde{n}_l^2 \alpha_{\text{MEC}}}{(\chi_{\text{MEC}} \beta_l)^2}$.⁵

For the compression time, we let $\kappa \in [1, \kappa_{\text{max}}]$ denote the compression ratio, which is the ratio of the size of raw data to the size of compressed data. κ_{max} is the maximum compression ratio. Let X_c denote the number of CPU cycles for compressing 1-bit data, which follows $\text{Gamma}(\alpha_{\text{RA}}, \beta_c)$, where α_{RA} and β_c denote the shape and rate parameters of compression latency, respectively. There are two main existing conclusions to evaluate the expected computation load with the given compression ratio. The first one shows that

$$\mathbb{E}\{X_c\} = \frac{\alpha_{\text{RA}}}{\beta_c} = \exp(\psi\kappa) - \exp(\psi), \quad (21)$$

where $\psi > 0$ is a constant. This model can be used for several lossless compression techniques such as Zlib, Zstandard, and XZ compression [8], [9], [32]. Another conclusion shows that

$$\mathbb{E}\{X_c\} = \frac{\alpha_{\text{RA}}}{\beta_c} = \omega_1 (\omega_2 \kappa^{\omega_3} + \omega_4), \quad (22)$$

where ω_k , $k = 1, \dots, 4$ are the positive constants for lossless compression algorithms GZIP and BZ2 as shown in [33].⁶ Let $\zeta_c(\kappa) = \mathbb{E}\{X_c\}$, which is an increasing function of κ .

Let X_d denote the number of CPU cycles for decompressing 1-bit data. X_d follows $\text{Gamma}(\alpha_{\text{MEC}}, \beta_d)$, where β_d is the rate parameter of decompression latency. Accordingly, there are two main conclusions in the existing works to evaluate $\mathbb{E}\{X_d\}$. The first one shows that

$$\mathbb{E}\{X_d\} = \frac{\alpha_{\text{MEC}}}{\beta_d} = \omega_0 (\exp(\psi\kappa) - \exp(\psi)), \quad (23)$$

where $\omega_0 \in (0, 1)$ is a constant. Another conclusion shows

$$\mathbb{E}\{X_d\} = \frac{\alpha_{\text{MEC}}}{\beta_d} = \omega_5 (\omega_6 \kappa^{\omega_7} + \omega_8), \quad (24)$$

⁵Note that the analysis in this paper is also valid for GPU scenarios if the distribution of X_l^{cp} for GPU is given.

⁶Note that this model can also be used for evaluating $\mathbb{E}\{X_c\}$ of the lossy compression [33], e.g., JPEG.

where ω_5 , ω_6 , and ω_8 are positive constants. The sign of ω_7 is determined by the specific compression algorithms [33]. Let $\zeta_d(\kappa) = \mathbb{E}\{X_d\}$.

With the above models and definitions, $T_{ET}^c = \frac{n_{ET} X_c}{\chi_{RA}}$, and $T_{ET}^d = \frac{n_{ET} X_d}{\kappa \chi_{MEC}}$, where χ_{RA} is the frequency of the processing unit at RA. Thus, we obtain $T_{ET}^c \sim \text{Gamma}(\alpha_{RA}, \frac{\chi_{RA} \alpha_{RA}}{n_{ET} \zeta_c(\kappa)})$, with expectation $\mu_{ET}^c = \frac{n_{ET} \zeta_c(\kappa)}{\chi_{RA}}$ and variance $\xi_{ET}^c = \frac{(n_{ET} \zeta_c(\kappa))^2}{\chi_{RA}^2 \alpha_{RA}}$. $T_{ET}^d \sim \text{Gamma}(\alpha_{MEC}, \frac{\chi_{MEC} \alpha_{MEC} \kappa}{n_{ET} \zeta_d(\kappa)})$, with expectation $\mu_{ET}^d = \frac{n_{ET} \zeta_d(\kappa)}{\chi_{MEC} \kappa}$ and variance $\xi_{ET}^d = \frac{(n_{ET} \zeta_d(\kappa))^2}{(\chi_{MEC} \kappa)^2 \alpha_{MEC}}$.

B. Formulation of a Unified Optimization Problem

In this subsection, we will formulate a unified optimization problem for this CGC system, in which average-based and tail-based optimization objectives and constraints are considered.

The objective of the optimization can be set from various aspects. If we aim to reduce the closed-loop latency to improve reliability and provide a better experience for users, the objective function is related to the closed-loop latency T . If we aim to save resources, e.g., power and bandwidth, to ensure the performance of the CGC system, the objective function is related to the average power and bandwidth.

For the first kind of objective functions, we can also consider two cases, i.e., the average-based and tail-based objectives. The average-based objective is related to $\mathbb{E}\{T\}$. For the tail-based objective, let T_{th} denote the threshold for the closed-loop latency, which is determined by the specific applications and human's requirements. Thus, the tail-based objective is related to $\Pr\{T < T_{th}\}$. We let $d(T)$ denote the objective functions that are related to T . Besides, we let $g(P_{avg}, B)$ denote the objective functions related to resources. We also assume that $d(T)$ and $g(P_{avg}, B)$ are normalized.

A unified optimization problem for this CGC system is then formulated by combining different kinds of objectives and constraints.

$$\min \quad \varepsilon d(T) + (1 - \varepsilon) g(P_{avg}, B) \quad (25a)$$

$$\text{s.t.} \quad \text{Constraints of a vertex in Fig. 3,} \quad (25b)$$

$$P_{PF1} + P_{CD} \leq P_{RA}^{th}, \quad (25c)$$

$$P_{PF2} + P_{VI} \leq P_{BS}^{th}, \quad (25d)$$

$$B_{PF} + B_{ET} = B, \quad (25e)$$

where $\varepsilon \in [0, 1]$, P_{RA}^{th} and P_{BS}^{th} are the constraints of the average power on BS and RA, $B_{PF1} = B_{PF2} = B_{PF}$, and B (in Hz) is the maximum available bandwidth. For $\varepsilon = 0$, we are interested in designing a resource-efficient scheduling. For $\varepsilon = 1$, we focus on optimizing the performance of closed-loop latency. The optimization variables in this problem may include $\{\kappa, B_{PF}, B_{ET}, P_{PF1}, P_{PF2}, \tau_{PF1}, \tau_{PF2}, P_{CD}, P_{VI}\}$.

It is not trivial work to solve this optimization problem in CGC systems. As shown in Section III-A, we know the expectation and variance of each latency component in this system, which can be used to characterize some constraints related to the expectation and variance of T_{ET} . However, no matter which vertex's constraints are adopted, we have to obtain the distribution of closed-loop and FL's latency. For

vertices 2 and 4, we also need to obtain the CDF of CL latency. Since the latency of CL, FL, and closed loop are sums of gamma and negative binomial random variables, it is hard to obtain analytical distributions of the CL, FL, and closed-loop latency. Thus, it is crucial to derive the analytical expression for the distribution of CL, FL, and closed-loop latency for general scenarios to provide instructions for efficient performance evaluation or optimization.

IV. ANALYTICAL EXPRESSION OF THE LATENCY DISTRIBUTION IN CGC SYSTEMS

In this section, we will present a general method for approximating the distribution of CL, FL, and closed-loop latency. Based on this general method, we also present methods for efficiently evaluating the terms in different constraints. Since there are similarities in the latency distribution and constraints in CL, FL, and closed-loop latency, we will take FL for example to show how to derive the analytical expression for the terms in the proposed constraints for FL. Then we will also give the results of CL and closed-loop latency without detailed proofs. For simplicity, we define $T_1 = T_{CL} + T_{ET}$. Without loss of generality, we let $t_{CD} = t_{VI} = t_u$.

A. A General Method for Analytical Approximation for the CDF of Latency

From Section III, we find that there are discrete and continuous random variables in the components of CL, FL, and closed-loop latency. We have to treat them separately since they have different properties. We will first present a general method to approximate the CDF of T_{ET} , which can be applied to the CDF approximation of T_{CL} , T_{FL} , and T .

In Lemma 1, we obtain the analytical expression for the CDF of $T_{ET}^c + T_{ET}^d + T_{VI}^{cp}$ with the help of SPA, which is a sum of continuous random variables. For simplicity, let $F_1(x)$ and $f_1(x)$ denote the CDF and PDF of $T_{ET}^c + T_{ET}^d + T_{VI}^{cp}$, respectively. Besides, we let

$$\iota_1 = \left(\frac{n_{ET}^2 \zeta_c^2(\kappa)}{\chi_{RA}^2 \alpha_{RA}} + \frac{n_{ET}^2 \zeta_d^2(\kappa)}{\chi_{MEC}^2 \kappa^2 \alpha_{MEC}} + \frac{n_{ET}^2 \alpha_{MEC}}{\chi_{MEC}^2 \beta_{VI}^2} \right)^{\frac{3}{2}}, \quad (26)$$

$$\iota_2 = \frac{2n_{ET}^3 \zeta_c^3(\kappa)}{\chi_{RA}^3 \alpha_{RA}^2} + \frac{2n_{ET}^3 \zeta_d^3(\kappa)}{\kappa^3 \chi_{MEC}^3 \alpha_{MEC}^2} + \frac{2\alpha_{MEC} n_{ET}^3}{\chi_{MEC}^3 \beta_{VI}^3}, \text{ and } \quad (27)$$

$$\theta = \frac{n_{ET} \alpha_{MEC}}{\chi_{MEC} \beta_{VI}} + \frac{n_{ET} \zeta_c(\kappa)}{\chi_{RA}} + \frac{n_{ET} \zeta_d(\kappa)}{\chi_{MEC} \kappa}. \quad (28)$$

Lemma 1. With θ defined in Eq. (28),

- the CDF of $T_{ET}^c + T_{ET}^d + T_{VI}^{cp}$ is approximated by

$$F_1(x) = \begin{cases} \Phi(v_x) + \phi(v_x) \left(\frac{1}{v_x} - \frac{1}{u_x} \right), & x \neq \theta, \\ \frac{1}{2} + \frac{\iota_2}{6\sqrt{2}\pi\iota_1}, & x = \theta, \end{cases} \quad (29)$$

where

$$v_x = \text{sign}(\Xi_1(x)) \sqrt{2x\Xi_1(x) - 2L(\Xi_1(x))}, \text{ and } \quad (30)$$

$$u_x = \Xi_1(x) \sqrt{L''(\Xi_1(x))}.$$

$\Xi_1(\cdot)$ is the inverse function of $L'(\cdot)$. ι_1 and ι_2 are given in Eqs. (26) and (27), respectively. $L(\cdot)$ is given in Eq. (32), where $s < \min \left\{ \frac{\chi_{RA} \alpha_{RA}}{n_{ET} \zeta_c(\kappa)}, \frac{\chi_{MEC} \alpha_{MEC} \kappa}{n_{ET} \zeta_d(\kappa)}, \frac{\chi_{MEC} \beta_{VI}}{n_{ET}} \right\}$.

- the PDF of $T_{ET}^c + T_{ET}^d + T_{VI}^{cp}$ is approximated by

$$f_1(x) = \frac{\exp(L(\Xi_1(x)) - x\Xi_1(x))}{\sqrt{2\pi L''(\Xi_1(x))}}, \quad x > 0. \quad (33)$$

Proof: See Appendix A. ■

In Lemma 1, we derive the CDF and PDF of $T_{ET}^c + T_{ET}^d + T_{VI}^{cp}$, which is the sum of continuous components of T_{ET} . For T_1 , the sum of continuous components is $T_{LL}^{cp} + T_{ET}^c + T_{ET}^d + T_{VI}^{cp}$. Thus, we define $\tilde{L}(s)$ as

$$\tilde{L}(s) = L(s) - \alpha_{MEC} \ln \left(1 - \frac{N_{HL} n_{HL} s}{\chi_{MEC} \beta_{LL}} \right), \quad (34)$$

where $s < \min \left\{ \frac{\chi_{MEC} \beta_{LL}}{N_{HL} n_{HL}}, \frac{\chi_{RA} \alpha_{RA}}{n_{ET} \zeta_c(\kappa)}, \frac{\chi_{MEC} \alpha_{MEC} \kappa}{n_{ET} \zeta_d(\kappa)}, \frac{\chi_{MEC} \beta_{VI}}{n_{ET}} \right\}$.

Besides, we let $\tilde{l}_1 = \left(\iota_1^{\frac{2}{3}} + \frac{N_{HL}^2 n_{HL}^2 \alpha_{MEC}}{\chi_{MEC}^2 \beta_{LL}^2} \right)^{\frac{3}{2}}$, $\tilde{l}_2 = \iota_2 + \frac{2\alpha_{MEC} N_{HL}^3 n_{HL}^3}{\chi_{MEC}^3 \beta_{LL}^3}$, and $\tilde{\theta} = \theta + \frac{N_{HL} n_{HL} \alpha_{MEC}}{\chi_{MEC} \beta_{LL}}$. By replacing $\tilde{L}(s)$, \tilde{l}_1 , \tilde{l}_2 , and $\tilde{\theta}$ into Eqs. (29) and (33), we obtain the CDF and PDF of $T_{LL}^{cp} + T_{ET}^c + T_{ET}^d + T_{VI}^{cp}$. We let $\tilde{F}_1(x)$ denote the CDF of $T_{LL}^{cp} + T_{ET}^c + T_{ET}^d + T_{VI}^{cp}$.

In Lemma 2, we obtain the closed-form expression for the probability mass function (PMF) of $T_{CD}^{cm} + T_{VI}^{cm}$ with the help of saddlepoint mass functions, which is a sum of discrete components of T_{ET} . For simplicity, let p_k denote $\Pr\{T_{CD}^{cm} + T_{VI}^{cm} = kt_u\}$, where $k \in \{N_{CD} + N_{VI}, N_{CD} + N_{VI} + 1, \dots\}$.

Lemma 2 The PMF of $T_{CD}^{cm} + T_{VI}^{cm}$ is approximated by

$$p_k = \begin{cases} (1 - \epsilon_{CD})^{N_{CD}} (1 - \epsilon_{VI})^{N_{VI}}, & k = N_{CD} + N_{VI}, \\ \frac{\exp(J(\Xi_2(k)) - k\Xi_2(k))}{\sqrt{2\pi \left(\frac{\epsilon_{CD} N_{CD} e^{\Xi_2(k)}}{(1 - \epsilon_{CD} e^{\Xi_2(k)})^2} + \frac{\epsilon_{VI} N_{VI} e^{\Xi_2(k)}}{(1 - \epsilon_{VI} e^{\Xi_2(k)})^2} \right)}}, & k > N_{CD} + N_{VI}, \end{cases} \quad (35)$$

where $\Xi_2(\cdot)$ is the inverse function of $J'(\cdot)$. $J(\cdot)$ is given in Eq. (36).

Proof: See Appendix B. ■

In Lemma 2, we derive the PMF of $T_{CD}^{cm} + T_{VI}^{cm}$, which is the sum of discrete components of T_{ET} . For T_1 , the sum of discrete components is $T_{HL}^{cm} + T_{LL}^{cm} + T_{CD}^{cm} + T_{VI}^{cm}$. We let \tilde{p}_k denote $\Pr\{T_{HL}^{cm} + T_{LL}^{cm} + T_{CD}^{cm} + T_{VI}^{cm} = kt_u\}$. Moreover, we let $\tilde{J}(s)$ denote the CGF of $T_{HL}^{cm} + T_{LL}^{cm} + T_{CD}^{cm} + T_{VI}^{cm}$. Due to the layout limitation, we omit the expression of $\tilde{J}(s)$, which is similar to Eq. (36). By substituting $\tilde{J}(s)$ into Eq. (35), we obtain \tilde{p}_k , where $k > N_{HL} + N_{LL} + N_{CD} + N_{VI}$. For $k = N_{HL} + N_{LL} + N_{CD} + N_{VI}$, we have

$$\tilde{p}_k = (1 - \epsilon_{HL})^{N_{HL}} (1 - \epsilon_{LL})^{N_{LL}} p_{N_{CD} + N_{VI}}. \quad (36)$$

Moreover, we also let p_k^{CL} denote the PMF of $T_{HL}^{cm} + T_{LL}^{cm}$, which is the sum of discrete component of T_{CL} . Due to the layout limitation, we omit the derivation of p_k^{CL} , which is also similar to Eq. (35).

Based on Lemmas 1 and 2, we can derive the CDF of T_{CL} ,

T_{ET} , T_{FL} , T_1 and T in general scenarios. We let $F_{CT}(x)$, $F_{ET}(x)$, $F_{FL}(x)$, $F_{T_1}(x)$ and $F_T(x)$ denote the CDF of T_{CL} , T_{ET} , T_{FL} , T_1 , and T , respectively.

Theorem 1. For vertices 2, 4, 6, and 8, the CDF of T_{CL} is given by

$$F_{CL}(x) = \sum_{k=N_{HL}+N_{LL}}^{\lfloor \frac{x}{t_u} \rfloor} \frac{p_k^{CL}}{\Gamma(\alpha_{MEC})} \gamma \left(\alpha_{MEC}, \frac{\chi_{MEC} \beta_{LL}(x - kt_u)}{N_{HL} n_{HL}} \right), \quad (37)$$

where $x > 0$.

The CDF of T_{ET} is given by

$$F_{ET}(x) = \sum_{k=N_{CD}+N_{VI}}^{\lfloor \frac{x}{t_u} \rfloor} p_k F_1(x - kt_u), \quad x > 0. \quad (38)$$

The CDF of T_{FL} is given by

$$F_{FL}(x) = \mathbb{I}\{x < \tau_{PF}\} \frac{F_{ET}(x)}{1 - F_{ET}(\tau_{PF})}, \quad x > 0. \quad (39)$$

The CDF of T is given by

$$F_T(x) = \mathbb{I}\{x > \tau_{PF}\} F_{CL}(x - \tau_{PF}) F_{T_1}(x), \quad (40)$$

where $F_{T_1}(x)$ is given by

$$F_{T_1}(x) = \sum_{k=N_{HL}+N_{LL}+N_{CD}+N_{VI}}^{\lfloor \frac{x}{t_u} \rfloor} \tilde{p}_k \tilde{F}_1(x - kt_u), \quad x > 0. \quad (41)$$

Proof: The CDF of T_{CL} , T_{ET} , and T_1 can be obtained directly according to Lemmas 1 and 2. For T_{FL} , we can obtain its CDF based on $F_{ET}(x)$ and the definition of T_{FL} . For the closed-loop latency T , it can be expressed as $T = T_{CL} + T_{FL} = \max\{T_{CL} + \tau_{PF}, T_1\}$. Thus, the CDF of T is given by

$$\Pr\{T < x\} = \Pr\{T_{CL} < x - \tau_{PF}\} \Pr\{T_1 < x\}. \quad (42)$$

Then we obtain the CDF of T . ■

In Theorem 1, we derive the CDF of both CL, FL, and closed-loop latency. For practical applications, we can reduce the complexity of obtaining the approximation for $F_{ET}(x)$ by controlling the approximation accuracy. Based on Theorem 1, we conceive an algorithm for efficiently approximating $F_{ET}(x)$ in practical applications. The details of this algorithm are shown in Alg. 1. Steps 7 and 10 are used for normalizing the PMF of $T_{CD}^{cm} + T_{VI}^{cm}$. Similar procedures can be used to calculate $F_{CL}(x)$ and $F_{T_1}(x)$.

B. Continuous Approximation for a Large Number of Packets or Small Transmission Time of a Packet

In the last subsection, we present a general method to approximate the latency distribution. Since the CL, FL, and closed-loop latency consist of sums of continuous and discrete random variables, we adopt both the LR formula and saddlepoint mass function to obtain a satisfying approximation performance. However, in practical applications, the number of packets is usually large. Besides, the transmission time

$$L(s) = -\alpha_{RA} \ln \left(1 - \frac{n_{ET} \zeta_c(\kappa) s}{\chi_{RA} \alpha_{RA}} \right) - \alpha_{MEC} \ln \left(1 - \frac{n_{ET} \zeta_d(\kappa) s}{\chi_{MEC} \alpha_{MEC} \kappa} \right) - \alpha_{MEC} \ln \left(1 - \frac{n_{ET} s}{\chi_{MEC} \beta_{VI}} \right). \quad (32)$$

$$J(s) = N_{CD} (s + \ln(1 - \epsilon_{CD}) - \ln(1 - \epsilon_{CD} e^s)) + N_{VI} (s + \ln(1 - \epsilon_{VI}) - \ln(1 - \epsilon_{VI} e^s)), \quad s < \min\{-\ln \epsilon_{CD}, -\ln \epsilon_{VI}\}. \quad (36)$$

Algorithm 1 Calculating CDF of T_{ET}

Input: parameter $\Delta \in (0, 1)$ for controlling the approximation accuracy

Output: $F_{ET}(x)$

```

1: Initialization:  $k = N_{CD} + N_{VI} - 1$ ,  $\Theta = 0$ 
2: repeat
3:    $k \leftarrow k + 1$ 
4:   Calculate  $p_k$  according to Eq. (35)
5: until  $p_k < \Delta$ 
6:  $\nu \leftarrow \mathbb{I}\{k > N_{CD} + N_{VI}\} \sum_{i=N_{CD}+N_{VI}+1}^k p_i$ 
7: if  $\nu > 0$  then
8:   for all  $j = N_{CD} + N_{VI} + 1, \dots, k$  do
9:      $p_j \leftarrow (1 - p_{N_{CD}+N_{VI}}) \frac{p_j}{\nu}$ 
10:  end for
11: end if
12: if  $\left\lfloor \frac{x}{t_u} \right\rfloor < N_{CD} + N_{VI}$  then
13:    $\Theta \leftarrow 0$ 
14: else
15:   for all  $l = N_{CD} + N_{VI}, \dots, \min\left\{\left\lfloor \frac{x}{t_u} \right\rfloor, k\right\}$  do
16:     Calculate  $F_1(x - lt_u)$  according to Eq. (29).
17:      $\Theta \leftarrow \Theta + p_l F_1(x - lt_u)$ 
18:   end for
19: end if
20:  $F_{ET}(x) \leftarrow \Theta$ 

```

of a packet can be small in short-packet scenarios. In this subsection, we focus on these cases, in which the number of packets is large or t_u is small. Under this condition, we can use the central limit theorem (CLT) to approximate the sum of communication latency as normal random variables to turn T_{FL} and T into continuous random variables.

We start with the analysis for the discrete components of T_{ET} , which can be generalized to the analysis for the discrete components of T . T_{CD}^{cm} is the sum of N_{CD} i.i.d. random variables following geometric distribution, while T_{VI}^{cm} is similar. Under the condition that $N_{CD} + N_{VI}$ is large, $T_{CD}^{cm} + T_{VI}^{cm}$ can be approximated by a normal random variable. That is, $T_{CD}^{cm} + T_{VI}^{cm} \sim \mathcal{N}\left(\frac{N_{CD}t_u}{1-\epsilon_{CD}} + \frac{N_{VI}t_u}{1-\epsilon_{VI}}, \frac{\epsilon_{CD}N_{CD}t_u^2}{(1-\epsilon_{CD})^2} + \frac{\epsilon_{VI}N_{VI}t_u^2}{(1-\epsilon_{VI})^2}\right)$. As analyzed in [8], we are interested in the scenario in which the negative value from Gaussian approximation has a negligible effect on the analysis. Moreover, T_{CD}^{cm} and T_{VI}^{cm} are both t_u -lattice random variables. Thus, we can treat T_{CD}^{cm} and T_{VI}^{cm} as continuous random variables when t_u is small. There are two possibilities for small t_u scenarios from the perspective of the number of packets. The first possible case is that the $N_{CD} + N_{VI}$ is small. Since t_u is also small, the corresponding transmission time has a small influence on the distribution of T . The second case is that the $N_{CD} + N_{VI}$ is large. Then we can treat it as a continuous random variable by CLT. In

summary, we can also use CLT to approximate the distribution of T_{CD}^{cm} and T_{VI}^{cm} with small t_u .

Based on this continuous approximation, we can directly obtain the CDF and PDF approximation of T_{ET} according to the LR formula. We define the following constants as

$$\Psi = \theta + \vartheta t_u, \quad (43)$$

where

$$\vartheta = \frac{N_{CD}}{1 - \epsilon_{CD}} + \frac{N_{VI}}{1 - \epsilon_{VI}}. \quad (44)$$

We also define that

$$\Upsilon = \left(\iota_1^{\frac{2}{3}} + \frac{\epsilon_{CD}N_{CD}t_u^2}{(1 - \epsilon_{CD})^2} + \frac{\epsilon_{VI}N_{VI}t_u^2}{(1 - \epsilon_{VI})^2} \right)^{\frac{3}{2}}. \quad (45)$$

Lemma 3. Under the condition that $N_{CD} + N_{VI}$ is large or t_u is small,

- the CDF of T_{ET} is approximated by

$$\hat{F}_{ET}(x) = \begin{cases} \Phi(r_x) + \phi(r_x) \left(\frac{1}{r_x} - \frac{1}{z_x} \right), & x \neq \Psi, \\ \frac{1}{2} + \frac{\iota_2}{6\sqrt{2\pi}\Upsilon}, & x = \Psi, \end{cases} \quad (46)$$

where

$$r_x = \text{sign}(\Xi_3(x)) \sqrt{2x\Xi_3(x) - 2M(\Xi_3(x))}, \text{ and } \quad (47)$$

$$z_x = \Xi_3(x) \sqrt{M''(\Xi_3(x))}.$$

$M(s)$ is given in Eq. (48). $\Xi_3(\cdot)$ is the inverse function of $M'(\cdot)$.

- the PDF of T_{ET} is approximated by

$$\hat{f}_{ET}(x) = \frac{\exp(M(\Xi_3(x)) - x\Xi_3(x))}{\sqrt{2\pi M''(\Xi_3(x))}}, x > 0. \quad (49)$$

Proof: The proof is similar to the proof of Lemma 1. The CGF is shown in Eq. (48). Ψ is the expectation of T_{ET} . It is obvious that $M'(s)$ is an increasing function of s . Thus, the inverse function of $M'(s)$ exists, which we denote by $\Xi_3(\cdot)$. Besides, we find that $M''(0)^{3/2} = \Upsilon$ and $M'''(0) = \iota_2$. Thus, we obtain Eq. (46). With the help of the saddlepoint density function, we obtain Eq. (49). ■

By combining CLT with SPA, we can directly obtain the CDF of T_{ET} . The same method can be applied to obtaining the CDF of T_1 with the condition that $N_{HL} + N_{LL} + N_{CD} + N_{VI}$ are large or t_u is small. Let $\tilde{M}(s)$ denote the CGF of T_1 , which is given in Eq. (50), where $s < \min\left\{\frac{\chi_{MEC}\beta_{LL}}{N_{HL}n_{HL}}, \frac{\chi_{RA}\alpha_{RA}}{n_{ET}\zeta_c(\kappa)}, \frac{\chi_{MEC}\alpha_{MEC}\kappa}{n_{ET}\zeta_d(\kappa)}, \frac{\chi_{MEC}\beta_{VI}}{n_{ET}}\right\}$. Besides, we also define $\tilde{\Psi}$ and $\tilde{\Upsilon}$ as follows

$$\tilde{\Psi} = \tilde{\theta} + \left(\vartheta + \frac{N_{HL}}{1 - \epsilon_{HL}} + \frac{N_{LL}}{1 - \epsilon_{LL}} \right) t_u. \quad (51)$$

$$\tilde{\Upsilon} = \left(\Upsilon^{\frac{2}{3}} + \frac{N_{HL}^2 n_{HL}^2 \alpha_{MEC}}{\chi_{MEC}^2 \beta_{LL}^2} + \frac{\epsilon_{CD}N_{CD}t_u^2}{(1 - \epsilon_{CD})^2} + \frac{\epsilon_{VI}N_{VI}t_u^2}{(1 - \epsilon_{VI})^2} \right)^{\frac{3}{2}}. \quad (52)$$

By substituting $\tilde{M}(s)$, $\tilde{\iota}_2$ (defined below Eq. (34)), $\tilde{\Psi}$, and

$$M(s) = L(s) + \vartheta t_u s + \frac{s^2}{2} \left(\frac{\epsilon_{CD}N_{CD}t_u^2}{(1 - \epsilon_{CD})^2} + \frac{\epsilon_{VI}N_{VI}t_u^2}{(1 - \epsilon_{VI})^2} \right), s < \min\left\{\frac{\chi_{RA}\alpha_{RA}}{n_{ET}\zeta_c(\kappa)}, \frac{\chi_{MEC}\alpha_{MEC}\kappa}{n_{ET}\zeta_d(\kappa)}, \frac{\chi_{MEC}\beta_{VI}}{n_{VI}}\right\}. \quad (48)$$

$$\tilde{M}(s) = M(s) - \alpha_{MEC} \ln\left(1 - \frac{N_{HL}n_{HL}s}{\chi_{MEC}\beta_{LL}}\right) + \left(\frac{N_{HL}t_u}{1 - \epsilon_{HL}} + \frac{N_{LL}t_u}{1 - \epsilon_{LL}} \right) s + \frac{s^2}{2} \left(\frac{\epsilon_{HL}N_{HL}t_u^2}{(1 - \epsilon_{HL})^2} + \frac{\epsilon_{LL}N_{LL}t_u^2}{(1 - \epsilon_{LL})^2} \right). \quad (50)$$

\hat{Y} into Eqs. (46) and (49), we can obtain $\hat{F}_{T_1}(x)$ and $\hat{f}_{T_1}(x)$, where $\hat{F}_{T_1}(x)$ and $\hat{f}_{T_1}(x)$ are the continuous approximation for the CDF and PDF of T_1 , respectively. We then present the continuous approximation for the CDF of T in Theorem 2.

Theorem 2. Under the condition that $N_{HL} + N_{LL} + N_{CD} + N_{VI}$ is large or t_u is small, the CDF of the closed-loop latency is approximated by

$$\hat{F}_T(x) = \mathbb{I}\{x > \tau_{PF}\} F_{CL}(x - \tau_{PF}) \hat{F}_{T_1}(x). \quad (53)$$

Note that if $N_{LL} + N_{HL}$ is large or t_u is small, we can also use the continuous approximation $\hat{F}_{CL}(x)$ to replace $F_{CL}(x)$ in Eq. (53). However, N_{LL} is usually equal to 1 in practical scenarios. Besides, T_{CL} only has three latency components, in which the CDF of T_{LL}^{cp} is known. Thus, we use the general approximation for the CDF of T_{CL} in Eq. (53) to ensure high accuracy while ensuring efficiency.

C. Efficient Evaluation for Different Kinds of Constraints and Properties for Optimization

In this subsection, we will propose the methods for evaluating some kinds of constraints efficiently with the help of conclusions in Sections IV-A and IV-B. Then, we will present some properties of the communication and computation processes in this system, which are useful for further optimization.

In Sections IV-A and IV-B, we have derived the CDF of T_{CL} , T_{ET} , T_{FL} , and T . Besides, we know the expectation and variance of each latency component in this system. Thus, all constraints mentioned in Section II-B can be characterized by the obtained conclusions. However, some constraints can be evaluated more efficiently. Thus, we present the efficient evaluating methods for these constraints by SPA-based methods.

Eq. (9) has a constraint for the conditional expectation $\mathbb{E}\{(T_{ET} - \tau_{PF})^+\}$. If we want to calculate it, the intuitive method is to use the PDF of T_{ET} . However, we can not obtain the PDF for the general case since T_{ET} may not be a continuous random variable. Besides, it seems possible to obtain $f_{ET}(x)$ by Eq. (49) from the perspective of theoretical analysis when $N_{CD} + N_{VI}$ are large or t_u is small. However, the closed-form expression of $\Xi_3(x)$ is hard to obtain in Eq. (49), which makes calculating $f_{ET}(x)$ in a continuous interval impossible. One possible method to approximate the PDF of T_{ET} is discretization as done in our previous work [22].

Though we can design a discrete approximation for the PDF of T_{ET} based on Lemma 3, it is computation-intensive since we have to solve SPA equations at a large number of points when granularity is small. Instead, we present an efficient method to derive $\mathbb{E}\{(T_{ET} - \tau_{PF})^+\}$ in Corollary 1.

Corollary 1. Under the condition that $N_{CD} + N_{VI}$ is large or t_u is small, $\mathbb{E}\{(T_{ET} - \tau_{PF})^+\}$ can be approximated by Eq. (54), where $\hat{F}_{ET}(\tau_{PF})$, $\hat{f}_{ET}(\tau_{PF})$, and $\Xi_3(\tau_{PF})$ are given in Lemma 3.

Proof: Corollary 1 is based on the Eq. (2) in [34]. However, this equation requires that the random variable

should be continuous. Therefore, we adopt the continuous approximation proposed in Section VI. ■

Based on Eq. (54) in Corollary 1, we can evaluate $\mathbb{E}\{(T_{ET} - \tau_{PF})^+\}$ by only calculating the CDF and PDF of T_{ET} at one point, which is more efficient than the discrete-approximation method.

Then, we turn our focus to Eq. (11). The communication latency of PF data is stochastic for this constraint. To calculate $\Pr\{|T_{ET} - T_{PF}| < \tau_{td}\}$, it is equivalent to calculate

$$\Pr\{T_{ET} - T_{PF} < \tau_{td}\} - \Pr\{T_{ET} - T_{PF} < -\tau_{td}\}. \quad (55)$$

Thus, we can use the similar method proposed in Theorem 1 to adopt the SPA-based method by first deriving the CGF of $T_{ET} - T_{PF}$. Due to the layout limitation, we omit the details.

Then, we want to provide some useful properties for optimizing the system's performance. For the PF data, we give a conclusion on the period allocation for the case with CSIRT and FSD to minimize the average power consumption for the PF data transmission. For the ET data, we present a conclusion related to the choice of compression ratio.

Lemma 4. For the case that the transmission of PF data with CSIRT and FSD, the period allocation to achieve a minimum $P_{PF1} + P_{PF2}$ is $\tau_{PF1} = \tau_{PF2} = \frac{\tau_{PF}}{2}$.

Proof: By rewriting Eq. (17), we obtain that

$$P_j = \frac{N_0 B_{PF}}{c_1 d_j^{-\ell_j}} \left(2^{\frac{R_j}{B_{PF}}} - 1 \right) (c_2 + (\tau_j)^{-c_3}). \quad (56)$$

It is obvious that P_j is a convex function of τ_j . Thus, we have the conclusion in Lemma 4 by solving a convex optimization problem. ■

Lemma 5. For $\zeta_d(\kappa)$ shown in Eqs. (23) and (24) with $\omega_7 > 1 + \frac{\omega_8}{\omega_6}$, $\frac{\kappa}{\zeta_d(\kappa)}$ is a decreasing function of κ . For $\zeta_d(\kappa)$ shown in Eq. (24) with $\omega_7 \leq 1$, $\frac{\kappa}{\zeta_d(\kappa)}$ is an increasing function of κ .

Proof: See Appendix C. ■

In Lemma 4, we show that it is resource-efficient to set equal deadlines for the transmission of PF data in two hops. In Lemma 5, we present conclusions for the monotonic properties of $\frac{\kappa}{\zeta_d(\kappa)}$, which is related to the distribution, expectation, and variance of T_{ET}^d . This conclusion can provide instructions for the choice of κ .

V. SIMULATION AND NUMERICAL RESULTS

In this section, we validate the proposed framework through Monte Carlo simulations and discuss the results from the perspective of the envisioned 6G scenarios. The parameters of the simulation and numerical calculations are mainly based on [8] and [32]. Specifically, we set $\alpha_{MEC} = 1.25$, $\alpha_{RA} = 1.5$, $\beta_{LL} = \beta_{VI} = 1$, $N_{HL} = 3$, $N_{LL} = 1$, $n_{HL} = 128$ KB, $\epsilon_{HL} = \epsilon_{LL} = 10^{-5}$, $\chi_{RA} = 5$ GHz, $\chi_{MEC} = 15$ GHz, $\Delta = 10^{-5}$, and $n_{ET} = 1$ MB. $\zeta_c(\kappa)$ and $\zeta_d(\kappa)$ follow Eq. (22) and Eq. (23), respectively, with $\psi = 3.5$ and $\omega_0 = 0.1$.

In Figs. 4-7, we present the simulation and numerical results of CDF of T_{ET} and T . In these figures, we let

$$\mathbb{E}\{(T_{ET} - \tau_{PF})^+\} \approx (\theta + \vartheta t_u - \tau_{PF}) \left(1 - \hat{F}_{ET}(\tau_{PF}) \right) + \frac{\tau_{PF} - \theta - \vartheta t_u}{\Xi_3(\tau_{PF})} \hat{f}_{ET}(\tau_{PF}), \quad \text{if } \tau_{PF} \neq \theta + \vartheta t_u. \quad (54)$$

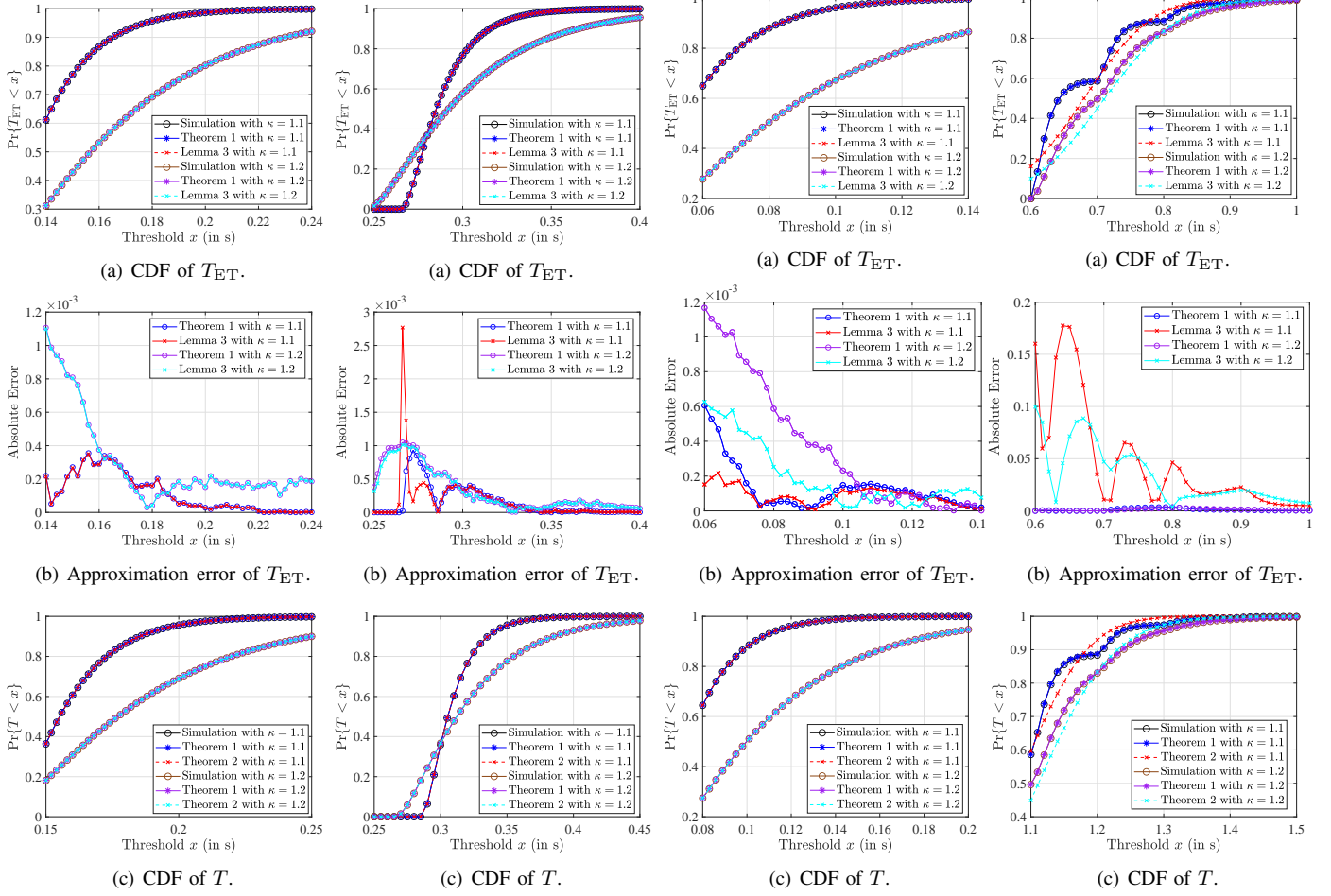


Fig. 4: T_{ET} and T with $t_u = 5$ ms, $N_{CD}^{(1,1)} = 20$, $N_{VI} = 3$, $\epsilon_{CD} = 10^{-3}$, and $\epsilon_{VI} = 10^{-4}$.

$N_{CD}^{(1,1)}$ denote the number of compressed-data packets with $\kappa = 1.1$. Thus, the number of compressed-data packets with $\kappa = 1.2$ is denoted by $N_{CD}^{(1,2)} = \left\lceil \frac{1.1}{1.2} N_{CD}^{(1,1)} \right\rceil$. The curves with the legend ‘Simulation’ refer to the Monte-Carlo simulation results averaged over 10^7 independent simulations, while the curves with the legend ‘Theorem 1’, ‘Lemma 3’, and ‘Theorem 2’ represent the numerical results of Alg. 1, Eq. (46), and Eq. (53), respectively. We considered four scenarios in Figs. 4-7. Fig. 4 represents the general scenario. Fig. 5 represents the scenario with a large number of packets. Fig. 6 represents the scenarios with a small t_u and a small number of packets. Fig. 7 represents the extreme scenario in which the number of packets is small and t_u is large. By comparing the simulation and numerical results, we find that both Theorem 1, Lemma 3, and Theorem 2 perform well in Figs. 4, 5, and 6. However, Theorem 1 performs much better than Lemma 3 in Fig. 7(a) and much better than Theorem 2 in Fig. 7(c). That is because, in Lemma 3 and Theorem 2, we adopted CLT to continuously approximate the CGF of T_{ET} and T . The results in these four figures validate the accuracy of Theorem 1. Besides, as we analyzed in Section IV, Lemma 3 can be applied when t_u is small or the number of packets is large. The results in Figs. 4, 5, and 6 show the effectiveness of Lemma 3 and Theorem

Fig. 5: T_{ET} and T with $t_u = 5$ ms, $N_{CD}^{(1,1)} = 50$, $N_{VI} = 3$, $\epsilon_{CD} = 10^{-3}$, and $\epsilon_{VI} = 10^{-4}$.

2. Note that we adopt $t_u = 5$ ms in Fig. 6, which should have a worse performance than $t_u < 5$ ms. This result also proves the accuracy of Lemma 3 and Theorem 2 since $t_u = 5$ ms has presented a good accuracy. The reason that Lemma 3 and Theorem 2 perform not well in Fig. 7 is that the discrete components of T_{ET} and T are dominant, which can be seen from curves of simulation results in Fig. 7. Except for the extreme scenario, we can use Lemma 3 and Theorem 2 for the CDF approximation with satisfying accuracy.

There are more interesting details. First, we find that Theorem 2 seems to perform better than Theorem 1 in some points. The main reason may be that we set a threshold Δ in Alg. 1, which limited the preciseness of the results. Second, from the results shown in Fig. 7, the curves of Theorem 1 match well with those of the simulation results. This result shows the universality of Theorem 1 even under the extreme scenario. Moreover, we see that with the increase of κ , the CDF is not always decreasing as shown in Figs. 5(a) and 5(c). This result shows there are difficulties in determining the optimal compression ratio since the CDF with a given threshold x is not monotonic with the increase of κ . However, when x is large, e.g., $1 - \Pr\{T_{ET} < x\}$ is small, the CDF decreases with the increase of κ . Since we mainly focus on the threshold with

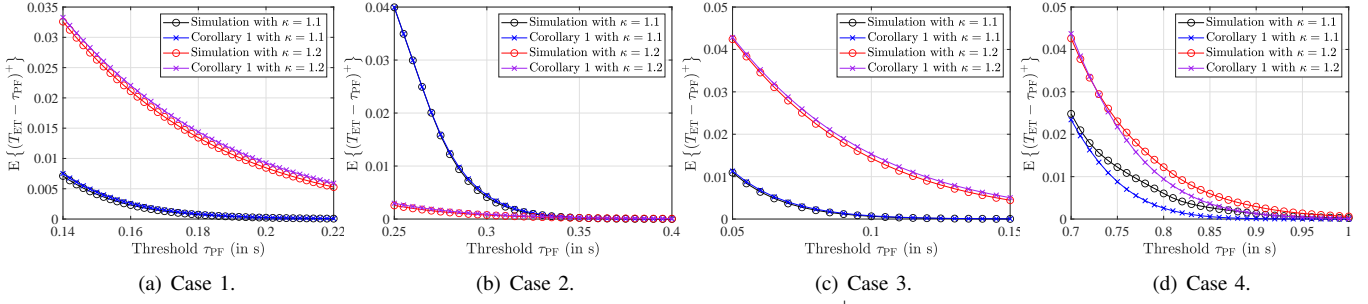


Fig. 8: Approximation of $\mathbb{E}\{(T_{ET} - \tau_{PF})^+\}$ versus τ_{PF} .

which $1 - \Pr\{T_{ET} < x\}$ is small, it is important to find and prove the condition that $1 - \Pr\{T_{ET} < x\}$ is decreasing with the increase of κ and a given x in the future work.

We then present the simulation and numerical results of $\mathbb{E}\{(T_{ET} - \tau_{PF})^+\}$ in Fig. 8. The parameter settings in Figs. 8(a)-(d) are identical with those in Figs. 4-7, respectively. The curves with the legend ‘Simulation’ refer to the Monte-Carlo simulation results averaged over 10^7 independent simulations, while the curves with the legend ‘Corollary 1’ represent the numerical results of Eq. (54). We find that the numerical results match well with the simulation results in Fig. 8(b). Thus, this result proves the effectiveness of Corollary 1. Moreover, the numerical results in Figs. 8(a) and 8(c) also provide satisfying performance. The difference between the numerical and simulation results becomes obvious in Fig. 8(d). For the extreme scenario shown in Fig. 8(d), we need a generalization of Eq. (54) to obtain an efficient and precise approximation for the conditional expectation, which is an important future work.

VI. CONCLUSION

In this paper, we focused on formulating a unified timing-analysis framework and proposing a general method to characterize the distribution of the closed-loop timing performance in CGC systems. The multi-modal feedback was divided into PF and ET data due to the heterogeneity of the feedback mechanism. Covering both timeliness, jitter, and reliability, we formulated a unified framework of timing analysis for CGC systems with different configurations, which includes average-based and tail-based constraints. The randomness of computation, compression, and communication were incorporated into the closed-loop timing analysis. To address the difficulties resulting from the sum of multiple random latency components, an SPA based method was conceived, which helped us derive the analytical expression of the closed-loop latency and other timing metrics. Important future topics include further optimization based on this unified framework, the introduction of emerging timing metrics into this framework, and the generalization of the approximation for the conditional expectation of timing metrics.

APPENDIX A PROOF OF LEMMA 1

The essence of the proof is to use the LR formula [20]. We first obtain the cumulant generating function (CGF) of $T_{ET}^c + T_{ET}^d + T_{VI}^{cp}$. The CGF of gamma random variable $X_1 \sim \text{Gamma}(\alpha, \beta)$ is given by

$$K_{X_1}(s) = -\alpha \ln \left(1 - \frac{s}{\beta} \right), \quad s < \beta. \quad (57)$$

Based on Eq. (57), we obtain the CGF of $T_{ET}^c + T_{ET}^d + T_{VI}^{cp}$, which is given in Eq. (32), where $s < \min \left\{ \frac{\chi_{RA}\alpha_{RA}}{n_{ET}\zeta_c(\kappa)}, \frac{\chi_{MEC}\alpha_{MEC}\kappa}{n_{ET}\zeta_d(\kappa)}, \frac{\chi_{MEC}\beta_{VI}}{n_{ET}} \right\}$. To obtain the CDF of $T_{ET}^c + T_{ET}^d + T_{VI}^{cp}$, we need to solve the saddlepoint equation to obtain the saddlepoint s_x . The saddlepoint equation is given by $L'(s_x) = x$, where $L'(s)$ is given by

$$L'(s) = \frac{\alpha_{RA}}{\frac{\chi_{RA}\alpha_{RA}}{n_{ET}\zeta_c(\kappa)} - s} + \frac{\alpha_{MEC}}{\frac{\chi_{MEC}\alpha_{MEC}\kappa}{n_{ET}\zeta_d(\kappa)} - s} + \frac{\alpha_{MEC}}{\frac{\chi_{MEC}\beta_{VI}}{n_{ET}} - s}. \quad (58)$$

$L'(s_x)$ is an increasing function of s_x . Thus, the inverse function of $L' : s_x \mapsto x$ exists, which is denoted by $\Xi_1 : x \mapsto s_x$. There is a unique solution of the saddlepoint equation, i.e., $\Xi_1(x)$, which can be solved by binary search.

Then, we divide the following proof into two cases. Let $\theta = \mathbb{E}\{T_{ET}^c + T_{ET}^d + T_{VI}^{cp}\}$ as shown in (28). The first case is that $x \neq \theta$ holds. According to the LR formula, we obtain

$$F_1(x) = \Phi(v_x) + \phi(v_x) \left(\frac{1}{v_x} - \frac{1}{u_x} \right), \quad (59)$$

where $v_x = \text{sign}(s_x) \sqrt{2(xs_x - L(s_x))}$, and $u_x = s_x \sqrt{L''(s_x)}$. The second-order derivative of $L(s)$ is given by

$$L''(s) = \frac{\alpha_{RA}}{\left(\frac{\chi_{RA}\alpha_{RA}}{n_{ET}\zeta_c(\kappa)} - s \right)^2} + \frac{\alpha_{MEC}}{\left(\frac{\chi_{MEC}\alpha_{MEC}\kappa}{n_{ET}\zeta_d(\kappa)} - s \right)^2} + \frac{\alpha_{MEC}}{\left(\frac{\chi_{MEC}\beta_{VI}}{n_{ET}} - s \right)^2}. \quad (60)$$

Thus, by substituting Eqs. (32) and (60) into the expressions of v_x and u_x , we obtain the first expression in Eq. (29).

The second case is that $x = \theta$ holds. Under this condition, $\Pr\{T_{ET} < x\}$ is given by

$$F_1(x) = \frac{1}{2} + \frac{L'''(0)}{6\sqrt{2\pi}L''(0)^{3/2}}. \quad (61)$$

We let $\iota_1 = L''(0)^{3/2}$ and $\iota_2 = L'''(0)$, which are given in Eqs. (26) and (27), respectively. By substituting Eqs. (26) and (27) into Eq. (61), we obtain Eq. (29).

For the PDF, we adopt the saddlepoint density functions in [20]. By substituting Eqs. (32) and (60) into the expression of the saddlepoint density function, we obtain Eq. (33). Due to the layout limitation, we omit the proof.

APPENDIX B PROOF OF LEMMA 2

Similar to the proof of Lemma 1, we shall first obtain the CGF of $T_{CD}^{cm} + T_{VI}^{cm}$. The CGF of negative binomial random

variable $X_2 \sim \text{NB}(N, p)$ is given by

$$K_{X_2}(s) = N(s + \ln p - \ln(1 - (1 - p)e^s)), \quad (62)$$

where $s < -\ln(1 - p)$. Based on Eq. (62), we obtain the CGF of $T_{\text{CD}}^{\text{cm}} + T_{\text{VI}}^{\text{cm}}$, which is given by Eq. (36). The first-order derivative of $J(s)$ is thus given by

$$J'(s) = \frac{N_{\text{CD}}}{1 - \epsilon_{\text{CD}}e^s} + \frac{N_{\text{VI}}}{1 - \epsilon_{\text{VI}}e^s}, \quad (63)$$

where $s < \min\{-\ln \epsilon_{\text{CD}}, -\ln \epsilon_{\text{VI}}\}$. The saddlepoint equation is thus given by $J'(s_k) = k$. $J'(s_k)$ is an increasing function of s_k . Thus, the inverse function of $J' : s_k \mapsto x$ exists, which is denoted by $\Xi_2 : x \mapsto s_k$. The solution of the saddlepoint equation is thus given by $\Xi_2(k)$.

Based on Eq. (63), we can also obtain

$$J''(s) = \frac{\epsilon_{\text{CD}}N_{\text{CD}}e^s}{(1 - \epsilon_{\text{CD}}e^s)^2} + \frac{\epsilon_{\text{VI}}N_{\text{VI}}e^s}{(1 - \epsilon_{\text{VI}}e^s)^2}, \quad (64)$$

where $s < \min\{-\ln \epsilon_{\text{CD}}, -\ln \epsilon_{\text{VI}}\}$. According to the saddlepoint mass function [20], we obtain the PMF for $k > N_{\text{CD}} + N_{\text{VI}}$, which is the interior of the span of the support of $T_{\text{CD}}^{\text{cm}} + T_{\text{VI}}^{\text{cm}}$. For $k = N_{\text{CD}} + N_{\text{VI}}$, the probability can be simply obtained as $(1 - \epsilon_{\text{CD}})^{N_{\text{CD}}}(1 - \epsilon_{\text{VI}})^{N_{\text{VI}}}$.

APPENDIX C PROOF OF LEMMA 5

Let $G(\kappa) = \frac{\kappa}{\zeta_d(\kappa)}$. For $\zeta_d(\kappa)$ shown in Eq. (23), we obtain

$$\frac{dG(\kappa)}{d\kappa} = \frac{e^{\psi\kappa}(1 - \kappa) - e^{\psi}}{\omega_0(e^{\psi\kappa} - e^{\psi})}. \quad (65)$$

Since $\kappa \geq 1$, $\frac{dG(\kappa)}{d\kappa} < 0$. For $\zeta_d(\kappa)$ shown in Eq. (24), we have

$$\frac{dG(\kappa)}{d\kappa} = \frac{\omega_5\omega_6(1 - \omega_7)\kappa^{\omega_7} + \omega_5\omega_8}{(\omega_5(\omega_6\kappa^{\omega_7} + \omega_8))^2}. \quad (66)$$

From this equation, we can find that $\omega_5\omega_6(1 - \omega_7)\kappa^{\omega_7}$ is decreasing with κ when $\omega_7 > 1$. Thus, the maximum value of $\omega_5\omega_6(1 - \omega_7)\kappa^{\omega_7}$ is achieved at $\kappa = 1$ since $\kappa \geq 1$, which is $\omega_5\omega_6(1 - \omega_7)$. Thus, if $\omega_5\omega_6(1 - \omega_7)\kappa^{\omega_7} + \omega_5\omega_8 < 0$, i.e., $\omega_7 > 1 + \frac{\omega_8}{\omega_6}$, the maximum value of $\frac{dG(\kappa)}{d\kappa} < 0$.

For $\omega_7 \leq 1$, $\omega_5\omega_6(1 - \omega_7)\kappa^{\omega_7} \geq 0$. Thus, $\frac{dG(\kappa)}{d\kappa} > 0$.

REFERENCES

- [1] P. Popovski, F. Chiariotti, K. Huang, A. E. Kalør, M. Kountouris, N. Pappas, and B. Soret, "A perspective on time toward wireless 6G," *Proc. IEEE*, vol. 110, no. 8, pp. 1116–1146, Aug. 2022.
- [2] "Framework and overall objectives of the future development of IMT for 2030 and beyond," Recommendation ITU-R M.2160-0, Nov. 2023.
- [3] D. Gündüz, Z. Qin, I. E. Aguerri, H. S. Dhillon, Z. Yang, A. Yener, K. K. Wong, and C.-B. Chae, "Beyond transmitting bits: Context, semantics, and task-oriented communications," *IEEE J. Sel. Areas Commun.*, vol. 41, no. 1, pp. 5–41, Jan. 2023.
- [4] D. Gündüz, F. Chiariotti, K. Huang, A. E. Kalør, S. Kobus, and P. Popovski, "Timely and massive communication in 6G: Pragmatics, learning, and inference," *IEEE BITS Inf. Theory Mag.*, vol. 3, no. 1, pp. 27–40, Mar. 2023.
- [5] E. C. Strinati, P. Di Lorenzo, V. Sciancalepore, A. Aijaz, M. Kountouris, D. Gündüz, P. Popovski, M. Sana, P. A. Stavrou, B. Soret *et al.*, "Goal-Oriented and Semantic Communication in 6G AI-Native Networks: The 6G-GOALS Approach," 2024, *arXiv:2402.07573*. [Online]. Available: <https://arxiv.org/abs/2312.09007>.
- [6] M. Xu, W. C. Ng, W. Y. B. Lim, J. Kang, Z. Xiong, D. Niyato, Q. Yang, X. Shen, and C. Miao, "A full dive into realizing the edge-enabled metaverse: Visions, enabling technologies, and challenges," *IEEE Commun. Surveys Tuts.*, vol. 25, no. 1, pp. 656–700, 1st Quart., 2023.
- [7] "Feasibility Study on Localized Mobile Metaverse Services," V19.1.0, document 3GPP TR 22.856, Sep. 2023.
- [8] S. Suman, F. Chiariotti, Č. Stefanović, S. Došen, and P. Popovski, "Statistical characterization of closed-loop latency at the mobile edge," *IEEE Trans. Commun.*, vol. 71, no. 7, pp. 4391–4405, Jul. 2023.
- [9] D. Han, W. Chen, B. Bai, and Y. Fang, "Offloading optimization and bottleneck analysis for mobile cloud computing," *IEEE Transactions on Communications*, vol. 67, no. 9, pp. 6153–6167, Sept. 2019.
- [10] J. R. Lorch and A. J. Smith, "Improving dynamic voltage scaling algorithms with pace," *SIGMETRICS Perform. Eval. Rev.*, vol. 29, no. 1, p. 50–61, Jun. 2001.
- [11] E. Steinbach, S. Hirche, M. Ernst, F. Brandi, R. Chaudhari, J. Kammerl, and I. Vittorias, "Haptic communications," *Proc. IEEE*, vol. 100, no. 4, pp. 937–956, Apr. 2012.
- [12] K. Antonakoglou, X. Xu, E. Steinbach, T. Mahmoodi, and M. Dohler, "Toward haptic communications over the 5G tactile internet," *IEEE Commun. Surveys Tuts.*, vol. 20, no. 4, pp. 3034–3059, 4th Quart., 2018.
- [13] P. Popovski, "Time, simultaneity, and causality in wireless networks with sensing and communications," *IEEE Open J. Commun. Soc.*, vol. 5, pp. 1693–1709, Mar. 2024.
- [14] B. Kizilkaya, C. She, G. Zhao, and M. A. Imran, "Task-oriented prediction and communication co-design for haptic communications," *IEEE Trans. Veh. Tech.*, vol. 72, no. 7, pp. 8987–9001, Jul. 2023.
- [15] D. Wen, P. Liu, G. Zhu, Y. Shi, J. Xu, Y. C. Eldar, and S. Cui, "Task-oriented sensing, computation, and communication integration for multi-device edge AI," *IEEE Trans. Wireless Commun.*, vol. 23, no. 3, pp. 2486–2502, Mar. 2024.
- [16] D. Van Huynh, S. R. Khosravirad, A. Masaracchia, O. A. Dobre, and T. Q. Duong, "Edge intelligence-based ultra-reliable and low-latency communications for digital twin-enabled metaverse," *IEEE Wireless Commun. Lett.*, vol. 11, no. 8, pp. 1733–1737, Aug. 2022.
- [17] P. M. de Sant Ana, N. Marchenko, P. Popovski, and B. Soret, "Age of loop for wireless networked control systems optimization," in *Proc. IEEE Int. Symp. Pers. Indoor Mob. Radio Commun. (PIMRC)*, Sept. 2021.
- [18] J. Cao, X. Zhu, S. Sun, P. Popovski, S. Feng, and Y. Jiang, "Age of loop for wireless networked control system in the finite blocklength regime: Average, variance and outage probability," *IEEE Trans. Wireless Commun.*, vol. 22, no. 8, pp. 5306–5320, Aug. 2023.
- [19] L. Li, L. Yang, X. Guo, Y. Shi, H. Wang, W. Chen, and K. B. Letaief, "Delay analysis of wireless federated learning based on saddle point approximation and large deviation theory," *IEEE J. Sel. Areas Commun.*, vol. 39, no. 12, pp. 3772–3789, Dec. 2021.
- [20] R. W. Butler, *Saddlepoint approximations with applications*. Cambridge, U.K.: Cambridge Univ. Press, 2007, vol. 22.
- [21] A. Ö. Kislal, A. Lancho, G. Durisi, and E. G. Ström, "Efficient evaluation of the error probability for pilot-assisted URLLC with massive MIMO," *IEEE J. Sel. Areas Commun.*, vol. 41, no. 7, pp. 1969–1981, Jul. 2023.
- [22] L. Li, W. Chen, and K. B. Letaief, "On power-latency-throughput tradeoff of diversity enabled delay-bounded communications," in *Proc. IEEE Int. Conf. Commun. (ICC)*, Jun. 2023, pp. 2141–2146.
- [23] H. Cui, Y. Du, Q. Yang, Y. Shao, and S. C. Liew, "LLMind: Orchestrating AI and IoT with LLMs for Complex Task Execution," 2023, *arXiv:2312.09007*. [Online]. Available: <https://arxiv.org/abs/2312.09007>.
- [24] T. Kallehauge, P. Ramirez-Espinosa, A. E. Kalør, and P. Popovski, *Statistical Characterization of URLLC: Frequentist and Bayesian Approaches*. New York, NY, USA: John Wiley & Sons, Ltd, 2023, ch. 2, pp. 15–59.
- [25] L. Li, W. Chen, and K. B. Letaief, "Simple bounds on delay-constrained capacity and delay-violation probability of joint queue and channel-aware wireless transmissions," *IEEE Trans. Wireless Commun.*, vol. 22, no. 4, pp. 2744–2759, Apr. 2023.
- [26] L. Li, W. Chen, and K. B. Letaief, "Fitting Empowered Cross-Layer Scheduling for Real-Time Wireless Communications," accepted by *Proc. IEEE Int. Conf. Commun. (ICC)*, 2024.
- [27] M. Bennis, M. Debbah, and H. V. Poor, "Ultrareliable and low-latency wireless communication: Tail, risk, and scale," *Proc. IEEE*, vol. 106, no. 10, pp. 1834–1853, Oct. 2018.
- [28] C.-F. Liu, M. Bennis, M. Debbah, and H. V. Poor, "Dynamic task offloading and resource allocation for ultra-reliable low-latency edge computing," *IEEE Trans. Commun.*, vol. 67, no. 6, pp. 4132–4150, Jun. 2019.
- [29] L. Li, W. Chen, P. Popovski, and K. B. Letaief, "Reliability-Latency-Rate Tradeoff in Low-Latency Communications with Finite-Blocklength Coding," 2023, *arXiv:2309.06769*. [Online]. Available: <https://arxiv.org/abs/2309.06769>.
- [30] L. Li, W. Chen, and K. B. Letaief, "Ultra-reliable and low latency wireless communications with burst traffics: A large deviation method," in *Proc. IEEE Global Commun. Conf. (GLOBECOM)*, Dec. 2021.
- [31] L. Li, W. Chen, and K. B. Letaief, "Wireless Communications with Hard Delay Constraints: Cross-Layer Scheduling with Its Performance Analysis," *IEEE Internet Things J.*, major revision, 2024.
- [32] X. Li, C. You, S. Andreev, Y. Gong, and K. Huang, "Wirelessly powered crowd sensing: Joint power transfer, sensing, compression, and transmission," *IEEE J. Sel. Areas Commun.*, vol. 37, no. 2, pp. 391–406, Feb. 2019.
- [33] T. T. Nguyen, V. N. Ha, L. B. Le, and R. Schober, "Joint data compression and computation offloading in hierarchical fog-cloud systems," *IEEE Trans. Wireless Commun.*, vol. 19, no. 1, pp. 293–309, Jan. 2020.
- [34] Y. Zhang and Y. K. Kwok, "Saddlepoint approximations to tail expectations under non-gaussian base distributions: option pricing applications," *J. Appl. Stat.*, vol. 47, no. 11, pp. 1936–1956, 2020.